University of Zurich

Bachelor Thesis

Department of Physics
2024

Analysis of the radioactive decay rate of ^{60}Co

Author:
Amadeo Nalbantis

Supervisors:
Prof. Dr. Laura Baudis
Dr. Pin-Jung Chiu
Dr. Yannick Müller

30th May 2024

"Facts are stubborn, but statistics are more pliable."

Mark Twain

Abstract

Although the radioactive decay rate has long been considered constant for individual isotopes, modulations in radioactive decay rates have garnered attention in the realm of scientific research over the last decade, with several studies reporting intriguing observations of modulations. The University of Zurich (UZH) is one of the four locations, where data were collected over a period of five years as part of a larger experiment. Throughout the experiment, four distinct research facilities across three continents collaborated, conducting measurements on the decay rates of ^{44}Ti, ^{54}Mn, ^{137}Cs, and ^{60}Co. Additionally, environmental parameters including temperature, pressure, magnetic field, and humidity were recorded. In this bachelor's thesis, the focus lies on the evaluation of the data collected at UZH. A correlation study was conducted between the decay rate of ^{60}Co and the potential environmental influences. For this purpose, the Pearson and Spearman correlation coefficients between the decay rate and the environmental parameters were calculated. Additionally, the frequency spectrum of the rate was examined using Fourier transformation to detect possible modulations. No significant correlations between the decay rate and the environmental parameters was observed, and the frequency analysis of the data revealed the absence of dominant frequencies indicative of any modulation. The results indicate that there is no annual fluctuation in decay rates as suggested by one of the modulation observations. However, further approaches and methods such as moving average and alternative fitting models can be applied to provide a statistical limit on the potential amplitudes on the fluctuation of the decay rate. Also the datasets for the other isotopes, as well as the data from the other three universities, should be examined.

Contents

1 Introduction

Radioactive decay is one of the fundamental processes in nuclear physics. A multitude of decay modes are known. The common feature of these decays is their stochastic nature. This implies, it is not possible to predict when an individual atom will decay. Under the premise of pure stochasticity, the decay process is also independent of environmental influences. For a significant sample of identical elements, the overall decay rate can be modeled as a function of a parameter called half-life [1].

However, there are various research results indicating that there are seasonal fluctuations in the decay rates of radioactive isotopes. These modulations would imply that the half-life is not constant, contradicting the prevailing theory. For example, researchers at Brookhaven National Laboratory have found fluctuations in decay rates that exhibit a certain periodicity [2]. In addition, research groups have also postulated statistical correlations between decay rates and external factors. In a publication by Jenkins et al., a statistically significant correlation between the α- and β-decay rate of ^{32}Si and ^{226}Ra and the Earth-Sun distance is shown, which implies an annual modulation of the radioactive decay rates [3]. Multiple experiments have been carried out with the aim of confirming [4] or rejecting [5][6] the phenomenon of modulation of the rates. At the University of Zurich, a setup was installed, which measured the decay rates of ^{60}Co, ^{54}Mn, and ^{44}Ti [7]. Additionally, environmental parameters such as temperature, pressure, humidity, and magnetic field were monitored. The data were collected over the period of five years and subsequently processed. This bachelor thesis focuses on the analysis of the systematic effects of the environmental parameters on the rate of ^{60}Co. In chapter 2, essential elements of radioactive decay and the different decay modes are discussed. Chapter 3 provides a detailed explanation of the experimental setup and also explains how the raw data were collected. The focus of chapter 4 is on the frequency analysis using Fourier transformation, and various statistical evaluations on the systematic effects arising from environmental parameters. In chapter 5, the results are summarized and discussed. Potential next steps for further investigation are described in chapter 6.

2 Theoretical background

Radioactive decay is one of the most fundamental processes known in physics. It describes the transition of unstable nuclei into less energetic and therefore more stable configurations. There are multiple types of radioactive decays. Three of the most common types of decay are alpha-decay, beta-decay, and electron capture. Another type of decay is gamma-decay, which often follows an alpha- or beta-decay. However, unlike the other three types, in gamma-decay, the number of protons, electrons, and neutrons remains constant. In this chapter, a brief history of the discovery of radioactivity is first described, followed by the introduction of the different decay types related to our study in this work. In addition, the concept of half-life as well as activity, two important properties of radioactive decay, are introduced. Finally, the results of some important publications investigating modulations in decay rates are discussed.

2.1 Discovery of radioactive decay

In the second half of the 19th century, intensive research was conducted on the properties of materials and elements. In 1896, Henri Becquerel discovered the phenomenon of radioactivity by chance while examining the effects of light on uranium salts. This discovery piqued the interest of Marie and Pierre Curie. They further investigated the phenomenon described by Becquerel and eventually established the concept of radioactivity [8]. Additionally, they discovered two previously unknown radioactive elements - polonium and radium. For this work, they, along with Henri Becquerel, were awarded the Nobel Prize in 1903 [9].

2.2 Atomic stability and decay types

To make statements about the stability and decay modes of atoms, we define Z as the number of protons, N the number of neutrons, A the atomic mass number (total number of protons and neutrons in a nucleus), and $M(Z, A)$ the atomic mass as a function of Z and A [8].

A two-body radioactive decay can be viewed as a process in which an atom transitions from a higher energy state to a lower energy state (many-body-decays will not be further considered due to their relative rareness). Taking into account mass and energy conservation, it can be derived that the mass of the original atom must be greater than or equal to the mass of the daughter atom plus additional decay products including alpha-particles, electrons / positrons as well as electromagnetic waves in the form of photons

$$M(A, Z) \geq M(A', Z') + M_2. \tag{1}$$

In Eq. 1 A and Z are the values corresponding to the original atom, A' and Z' are the values for the daughter nucleus, and M_2 corresponds to the mass of additional decay products. Only a limited number of $M(A, Z)$-configurations can be considered stable. As shown in Fig. 1, the Z-N plane delineates distinct regions representing the stability and decay characteristics of atomic nuclei [[10],[8]].

2.2.1 Beta-decay

As displayed in Fig. 1, only a narrow band of Z-N configurations is considered to be stable. This region is characterized by a balanced proton-neutron ratio and is stable against β-decay and spontaneous fission. Spontaneous fission primarily occurs in heavy atomic nuclei [8]. Proton-unstable and neutron-unstable regions, positioned to the left and right of the stable region, denote nuclei prone to adjusting their proton-neutron ratio for a higher stability via a decay [10].

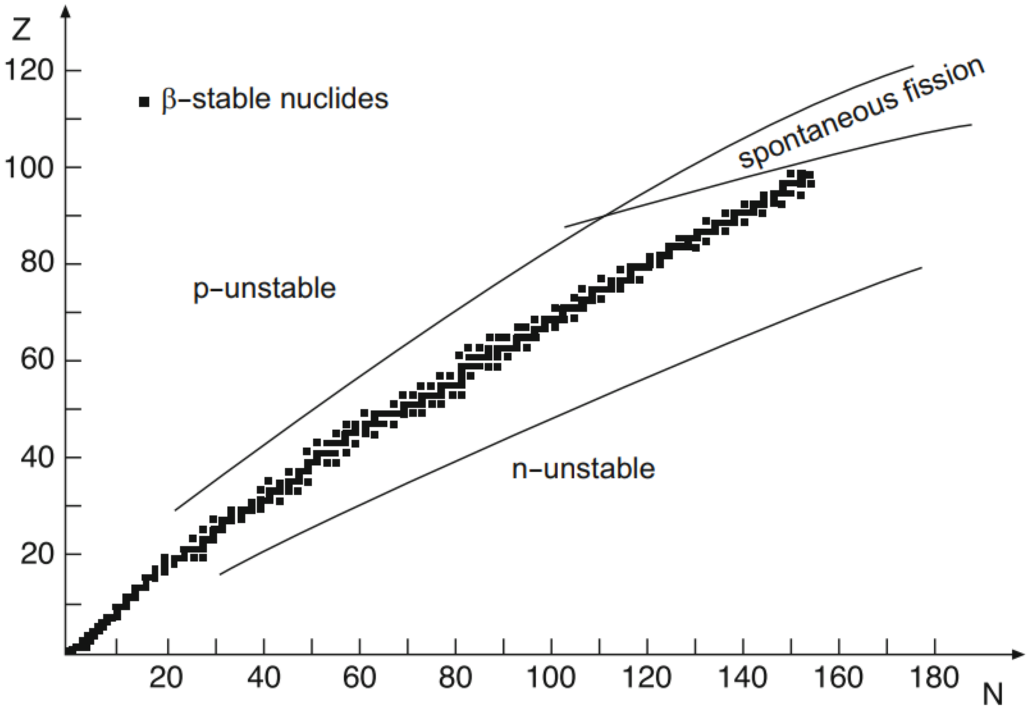

FIGURE 1: Z-N-plane with β-stable configurations. Figure from [10].

Isobaric atoms outside the stable band, with either a surplus of protons or neutrons, will decay via transitioning protons to neutrons or vice versa. This process is known as β decay.

In β^--decay, a neutron n is converted into a proton p, emitting an electron e^- and an electron antineutrino $\bar{\nu}_e$:

$$n \to p + e^- + \bar{\nu}_e. \tag{2}$$

In β^+-decay, a proton p is transformed into a neutron n, releasing a positron e^+ and an electron neutrino ν_e:

$$p \to n + e^+ + \nu_e. \tag{3}$$

For both decay types the total electric charge, the bayron number (number of protons and neutrons), the lepton number (number of electrons and neutrinos), as well as the total atomic mass number A are conserved [[8],[10]].

2.2.2 Electron capture

Electron capture is a nuclear process in which an atomic nucleus captures one of its own atomic electrons, typically from one of the closest orbitals surrounding the nucleus. During the process, an electron e^- combines with a proton p to form a neutron n. To ensure mass and lepton number conservation, an additional electron neutrino ν_e is released [10]. The general equation for electron capture can be represented as follows:

$$p + e^- \rightarrow n + \nu_e.$$

The condition for electron capture to occur is given by the following formula:

$$M(A, Z) \geq M(A, Z - 1) + \Delta E.$$

Here $M(A, Z)$ represents the mass of the parent nucleus with atomic number Z and mass number A, $M(A, Z - 1)$ represents the mass of the daughter nucleus with atomic number $Z - 1$ and mass number A, and ΔE represents the energy released during the electron capture process, which corresponds to the excitation energy in the daughter nucleus. Electron capture is particularly common in heavy atomic nuclei, where the electron orbit radii are small, and the likelihood of an electron being close enough to the nucleus for capture is relatively high [[1],[8]].

2.2.3 Alpha-decay

In alpha-decay, an unstable nucleus emits a positively charged $^4_2\mathrm{He}$ nucleus, consisting of two protons and two neutrons. This emitted particle is called α-particle. During alpha-decay, the parent nucleus ^A_ZX loses these four particles, resulting in a daughter nucleus ($^{A-4}_{Z-2}Y$) [[8],[1]]. The general equation for alpha decay can be represented as follows:

$$^A_ZX \rightarrow ^{A-4}_{Z-2} Y + ^4_2 \mathrm{He}.$$

Alpha-decay is a common mode of decay for heavy nuclei[10]. The large number of mutually repelling, positively charged protons in the nucleus counteracts the overall binding energy. Due to its high binding energy, the alpha-particle has increased kinetic energy and can escape the nucleus despite the Coulomb barrier, through the tunnel effect. This enables the nucleus to transition to a more energetically favorable state [8].

2.2.4 Gamma-decay

Gamma-decay involves the emission of photons (γ-particles) with short wavelengths from a nucleus in a state of excitation. Due to their short wavelengths, γ-particles are highly energetic. Unlike alpha- and beta-decays, gamma-decay has no effect on the atomic number Z or mass number A of the nucleus. Gamma-decay occurs whenever a nucleus in an excited states transitions to a lower energy state which usually happens alongside other types of decays, when the decay products are left in an excited state [8]

$$X^{Z^*}_A \rightarrow X^Z_A + \gamma. \tag{4}$$

2.3 Half-life and activity

The half-life of a radioactive substance, $t_{1/2}$, represents the duration needed for half of the radioactive nuclei within a sample to decay. It is a unique property of each radioactive nucleus and can vary widely for different elements and their isotopes. The concept of half-life is fundamental to understanding decay dynamics and is used in many scientific disciplines, such as radiometric dating, describing nuclear reactions, and determining the duration of medical treatments involving radioactive isotopes [8]. Radioactive decay is a stochastic process, which follows an exponential law [10]:

$$N(t) = N_0 \cdot e^{-\lambda t}, \tag{5}$$

where $N(t)$ is the number of radioactive nuclei at time t, which corresponds to the elapsed time between t_0 and t. N_0 is the initial number of radioactive nuclei at t_0, and λ is the decay constant. The decay constant is inversely proportional to the half-life and can be derived knowing that at $t = t_{\frac{1}{2}}$, the number of nuclei left is $\frac{N_0}{2}$. Hence,

$$\frac{N_0}{2} = N_0 e^{-\lambda t_{\frac{1}{2}}}.$$

Rearranging, we obtain:

$$e^{-\lambda t_{\frac{1}{2}}} = \frac{1}{2}.$$

Taking the natural logarithm on both sides and rearranging

$$-\lambda t_{\frac{1}{2}} = \ln\left(\frac{1}{2}\right)$$

$$t_{\frac{1}{2}} = -\frac{\ln\left(\frac{1}{2}\right)}{\lambda}.$$

Using $\ln\left(\frac{1}{2}\right) = -\ln(2)$, we obtain:

$$t_{\frac{1}{2}} = \frac{\ln(2)}{\lambda}.$$

And finally resulting in the equation for the half-life:

$$\lambda = \frac{\ln(2)}{t_{1/2}}. \tag{6}$$

Another important parameter is the activity of a radioactive substance. It describes how many decays occur at a given time t depending on the decay constant λ and $N(t)$,

$$A(t) = \lambda \cdot N(t). \tag{7}$$

It is often expressed in the unit becquerel (Bq), where 1 Bq corresponds to one decay per second [8],[1]].

2.4 Modulation in decay rates

As mentioned, radioactive decay is a stochastic process. Nevertheless, there were some observations that question this characteristic. Various experiments have been carried out to look for variations in decay rates of different isotopes. While some publications refute the hypothesis of variations in decay rates [[6],[5]], some claim the observation of seasonal modulations [[3],[4]]. The following section provides a brief overview of selected papers, describing the methods and the results obtained from different experiments. Table 1 provides a summary of the further discussed publications.

Year	Authors	Summary
2009	Jenkins et al.	Investigated both, α- and β- decays, of ^{32}Si and ^{226}Ra. They observed relative fluctuations in the amplitude of 0.3%. Different origins such as systematic errors but also effects of Earth-Sun-distances were discussed.
2009	Norman et al.	They investigated various sources and decay types, including alpha-, beta-decay, and electron capture. They focused on the correlations between the decay rates and the Earth-Sun distance. No significant correlations were observed.
2012	Bellotti et al.	They investigated beta-decay of ^{137}Cs. They detected no relative fluctuation in the amplitude of the activity larger than $9.6 \cdot 10^{-5}$.
2016	Alexeyev et al.	Found evidence of modulation correlated with lunar-daily as well as annual variations. They investigated the half-life of ^{214}Po, which mainly undergoes alpha-decay, and observed relative fluctuations in the normalized value of τ with amplitudes in the range of 6.9 - $8.9 \cdot 10^{-4}$.

Table 1: Overview of publications discussed in details in the following sections.

2.4.1 Publications supporting modulations in decay rates

In 2009 Jenkins et al. [3] concluded that there is a modulation in decay rates with a relative fluctuation of the amplitude of approximately 0.3%. They analyzed alpha- and beta-decays of ^{32}Si and ^{226}Ra. For their analysis they took the raw data from experiments previously conducted at the Brookhaven National Laboratory [2] as well as at the Physikalisch–Technische–Bundesanstalt in Germany [11]. It became evident that the observed fluctuations exhibit a strong correlation in time, not only between the two datasets but also with the seasons of the year. Two possibilities are discussed. On the one hand, they explain that these correlations may stem from seasonal influences on the detectors. On the other hand, they also discuss the possibility of an interaction of radioactive nuclei with the sun-emitted neutrino flux and other annual effects correlated with the variations in Earth-Sun distance as a reason for the observed modulations. However, they emphasize that further long-term experiments with different nuclides are necessary to determine the origins of the observed behaviors.

Alexeyev et al. [4] also supported the idea of annual modulations in decay rates. In their article, the authors presented a description of the TAU-2 setup, which was designed for a long-term study of the half-life of ^{214}Po, which mainly decays via alpha-decay. They investigated data collected over a period of 730 days and used different statistical methods such as moving average and χ^2-method for the analysis. Their analysis revealed various temporal variations for the values of τ. They obtained an average value for τ of 163.46 ± 0.04 μs. They observed annual, solar-daily, lunar-daily, and sidereal-daily fluctuations for a normalized value of τ with amplitudes in the range of $6.9 - 8.9 \cdot 10^{-4}$.

2.4.2 Publications refuting modulations in decay rates

In 2012, Bellotti et al. [6] found no evidence of modulation in decay rates. They monitored the activity of a ^{137}Cs source, which decays via beta-decay, between June 2011 and January 2012. They were using a HPGe detector situated at the Gran Sasso National Laboratory in Italy. Over 5100 hourly recorded energy spectra were taken over a span of 217 days. These extensive datasets facilitated the investigation of time variations in the decay constant across periods ranging from a few hours up to one year. To analyze the data a Fourier transformation as well as χ^2-analysis were used, and they detected no relative fluctuation in the amplitude larger than $9.6 \cdot 10^{-5}$. This upper limit is more than ten times lower than previously stated limits in existing literature.

Previously, Norman et al. [5] concluded in 2009 that there is no modulation in decay rates. As a direct response to the publication of Jenkins et al. [3], they revisited numerous datasets that were previously collected over a period of 15 years. They investigated possible correlations between the decay rates of ^{22}Na, ^{44}Ti, ^{108m}Ag, ^{121m}Sn, ^{133}Ba, and ^{241}Am, and to the Earth-Sun distance. They found no statistically significant evidence and set a constraint on the potential amplitudes of such correlations at a maximum of 0.06%.

3 Experimental setup

3.1 Modulation experiment

Zurich is one of four locations across three different continents where an identical experimental setup has been installed to gather data for further investigation of modulations in decay rates. In addition to Zurich, Purdue University in West Lafayette, Indiana, the US, the Dutch National Institute for Subatomic Physics (Nikhef) in Amsterdam, the Netherlands, and the Centro Brasileiro de Pesquisas Físicas (CBPF), in Rio de Janeiro, Brazil are part of this collaborative experiment. Table 2 summarizes the geographical information of the four setups. The varied geographical locations in the northern and the southern hemispheres serve to decouple laboratory systematics from seasonal effects. In each setup, three radioactive sources are investigated accompanied by the radioactive background measurements at each location [7].

Institute	Latitude	Longitude	Altitude (m)
Purdue	40.4259° N	86.9081° W	187
Nikhef	52.3564° N	4.9508° E	-3
Zurich	47.3743° N	8.5510° E	500
CBPF	22.9544° S	43.1676° W	16

TABLE 2: Geographical information of the experimental setups at the four institutions involved in the experiment. Table directly taken from Ref. [7].

Four different radioactive isotopes are being investigated in total. Each isotope is examined at a minimum of two out of the four locations. The half-lives of the isotopes and the institutes they are measured at are summarized in Tab. 3.

Source	Half-life	Institute
^{44}Ti	59.1(3) y	CBPF, Nikhef, Purdue, Zurich
^{54}Mn	312.2(2) d	Purdue, Zurich
^{60}Co	5.2712(4) y	CBPF, Nikhef, Purdue, Zurich
^{137}Cs	30.08(9) y	CBPF, Nikhef

TABLE 3: Isotopes, half-lives, and their corresponding locations. The half-lives were taken directly from Ref. [7].

For the measurement of the activity, two NaI(Tl) detectors are set up per radioactive source, each consisting of a NaI(Tl) scintillating crystal and a photomultiplier tube (PMT). Radiation emitted from the source excites the crystal. As the crystal de-excites, photons are emitted, which are then detected by the PMT [[12],[7]].

3.2 Photomultiplier tube

A photomultiplier tube (PMT) is a photon detection device that makes use of the photoelectric effect to convert incident photons into detectable electrical signals. Figure 2 illustrates the working principle of a PMT. A PMT comprises a photocathode, which emits electrons upon absorption of photons [13]. These emitted electrons undergo multiple stages of amplification facilitated by a series of dynodes. Through a process of secondary emission, each dynode amplifies the electron signal, leading to an exponential multiplication of produced electrons at each stage. The resulting amplified electron current is then collected at the anode, where it is converted into a measurable voltage output [14].

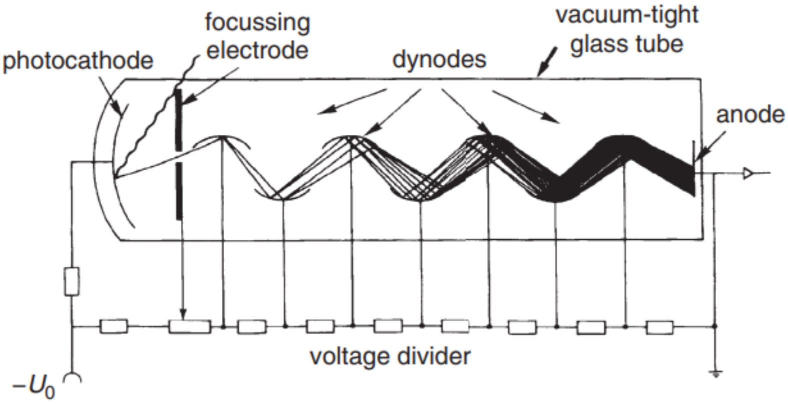

FIGURE 2: Schematic of the working principle of a PMT. The cathode absorbs photons and emits electrons. At each dynode the electron signal is amplified. At the anode the signal is converted to a measurable voltage output [13].

3.3 Experimental setup and data acquisition at the University of Zurich

The experimental setup involves the monitoring of three distinct radioactive sources. Each source is equipped with two NaI(Tl) detectors, composed of a scintillating NaI(Tl) crystal coupled to a PMT, positioned in opposing orientation to optimize data acquisition. To measure background radiation, an additional experimental arrangement without a radioactive source is installed. Figure 3 depicts three detection sets with a source located in between each detector pair and the fourth pair for background measurements, as well as a schematic of a single detection set with its corresponding source.

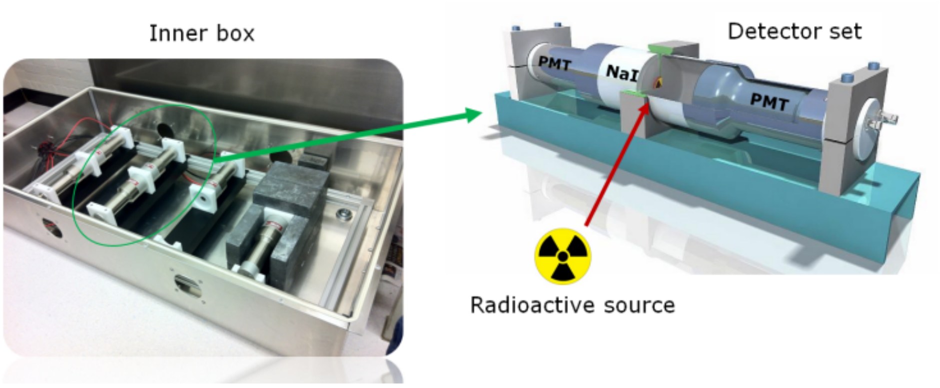

FIGURE 3: (Left): Inner box with four detector pairs and lead shielding (furthest right). (Right): Detailed depiction of a single detection set and a source [15].

To ensure minimal local variations from environmental parameters such as temperature, pressure, and humidity, the detector pairs are encapsulated in an airtight inner box. The inner box is insulated by a foam layer and the temperature is actively regulated with a heating system in order to maintain stable conditions [12]. Additionally, the inner box is filled with radio-pure nitrogen to mitigate the effects of radon radiation. To further minimize additional background radiation effects such as cosmic and terrestrial radiation as well as mutual effects from neighboring radioactive sources, the detectors are enclosed in a lead shield with a thickness of 5 cm [7]. Furthermore, to monitor the environmental conditions, various sensors recording pressure, temperature, humidity, and magnetic field were continuously taking measurements [[16],[12]]. Additionally, ^{222}Rn was measured, but due to a technical issue in processing the raw data, these values were unavailable and will not be discussed further in this thesis. The inner box is located in a protective outer box as shown in Fig. 4.

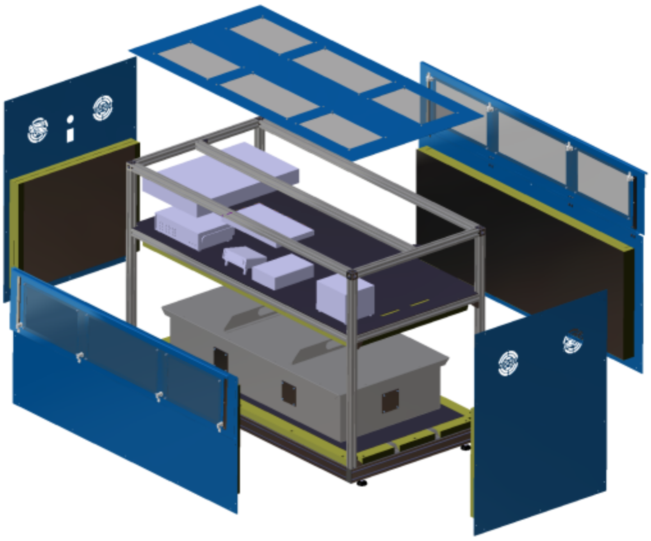

FIGURE 4: Schematic depiction of the outer box housing the inner box, data acquisition systems and various measurement devices.

The outer box houses two CAEN DT5533P [17] high-voltage supplies for the detectors, a NI-PXIe data acquisition system (DAQ), and a PID (Proportional-Integral-Derivative) heat controller [[16],[7]]. Each event, detected by a PMT, is stored in the DAQ as a waveform. The collected data are further processed, including the integration of the waveform and the calibration from electronic signals to physical units. The processed data include events on hourly bases with a distinct time stamp. Each event includes the rate (events per second) as well as the values of the environmental parameters [12]. These processed data were used as the base for what is discussed in this thesis. The experimental setup also includes a safety mechanism that cuts off the main power supply when temperature sensors detect values that deviate significantly from the predefined temperature range [15]. External connections include a 110 V power supply, a gas in-flow to regulate the nitrogen level of the inner box, and an Ethernet cable to export raw data for the processing[16].

Studies using data from the experimental setup described above have been conducted in the past. In 2018, Angevaare et al. examined the correlations between solar flares and the beta-decay rates of ^{60}Co, ^{44}Ti, and ^{137}Cs. They found no significant correlations and established a limit for possible relative fluctuations in the decay rates at 0.062% [18].

Each of the three radioactive isotopes is characterized by a distinctive decay scheme with multiple peaks in the corresponding energy spectrum. Table 4 provides an overview of the three radioactive sources that are used in the UZH setup. The column "channel number" corresponds to the ID of the detectors and the columns "peak" denote the energy levels of the individual decay schemes.

Source	Channel number	Peak 0 (keV)	Peak 1 (keV)	Peak 2 (keV)
^{60}Co	0, 1	1173.2	1332.5	2505.7
^{54}Mn	2, 3	834.8		
^{44}Ti	4, 5	511.00	1157.02	1668.02
Background	6, 7	1460		

TABLE 4: Sources, their distinct energy peaks, and corresponding channels/ detectors [12].

Figure 5 depicts the energy spectra for the three sources as well as the background radiation. For each plot in Fig. 5 there is a red and a blue line, which correspond to the two detectors used to measure each source. The raw data was binned into bins with a width of 5 keV during the processing. Consequently, the energy resolution is 5 keV. ^{60}Co and ^{44}Ti have three different peaks, whereas ^{54}Mn is observed to only have one peak at 834.8 keV. All datasets from all channels and peaks were examined beforehand. As most contain significant rate shifts and other anomalies that require further investigation, this thesis focuses exclusively on the data from the dataset where channel = peak = 0 from ^{60}Co at 1173.2 keV.

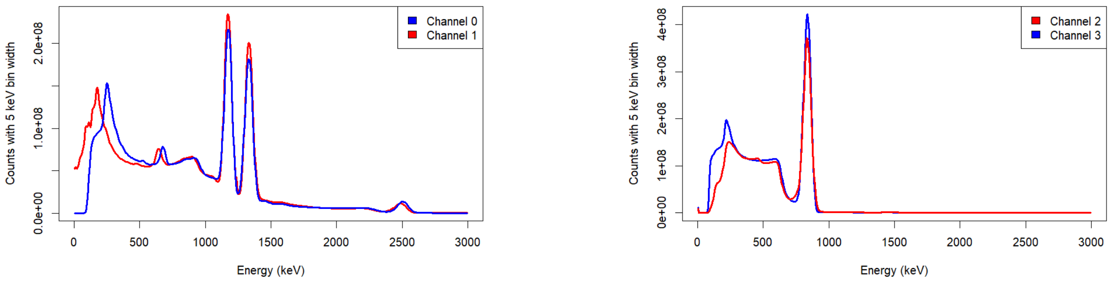

(A) Energy spectrum of ^{60}Co

(B) Energy spectrum of ^{54}Mn

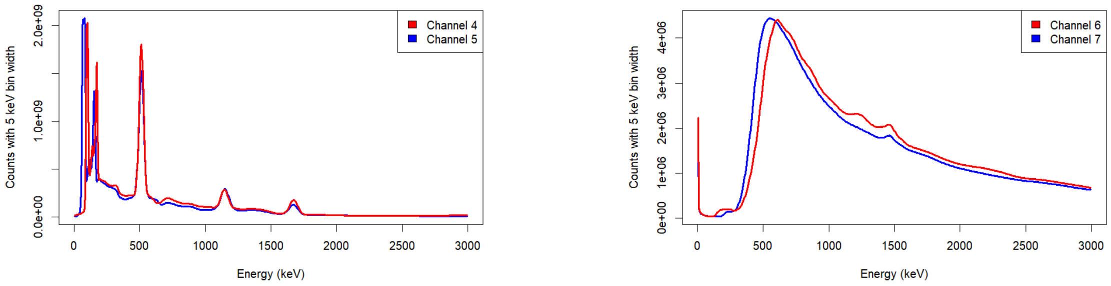

(C) Energy spectrum of ^{44}Ti

(D) Background energy spectrum

FIGURE 5: Energy spectra of the measurements from the eight PMT channels with three radioactive sources and environmental background (source: data of around five years of measurement). Note: y-axis corresponds to the number of events binned with a width of 5 keV.

4 Data analysis and results

In this chapter the preprocessed raw data are further treated by removing outliers in order to conduct further analyses. This treatment is defined as data cleaning. The goals are to examine correlations between the decay rate of the radioactive source and the environmental parameters and in additon to perform a Fourier transformation of the rate to investigate potential frequencies that would reinforce the concept of annual modulations in decay rates. The analysis was performed on the dataset of ^{60}Co at 1173.2 keV.

4.1 Data cleaning

First, all visually implausible / unphysical data points were removed. Next, an exponential model was fitted in order to calculate and analyze the residuals of the fitted model and the actual data. Following this, a threshold for data points whose residuals exceed a certain level was defined, classifying additional data points as outliers and removing them. Then, a second exponential function was fitted in order to determine the half-life from the fit parameters. Finally, the adjusted rate was introduced, which is the decay rate multiplied by the inverse of its corresponding exponential decay used to eliminate the decaying effect. The adjustement of the rate was needed to perform the Fourier transformation in order to investigate the frequency spectrum.

4.1.1 Decay rate

Figure 6 shows the preprocessed raw data over a period of almost five years. The range of the rate (number of decays per second) spans from 0 to 28. Some data points appear entirely implausible from a physical standpoint.

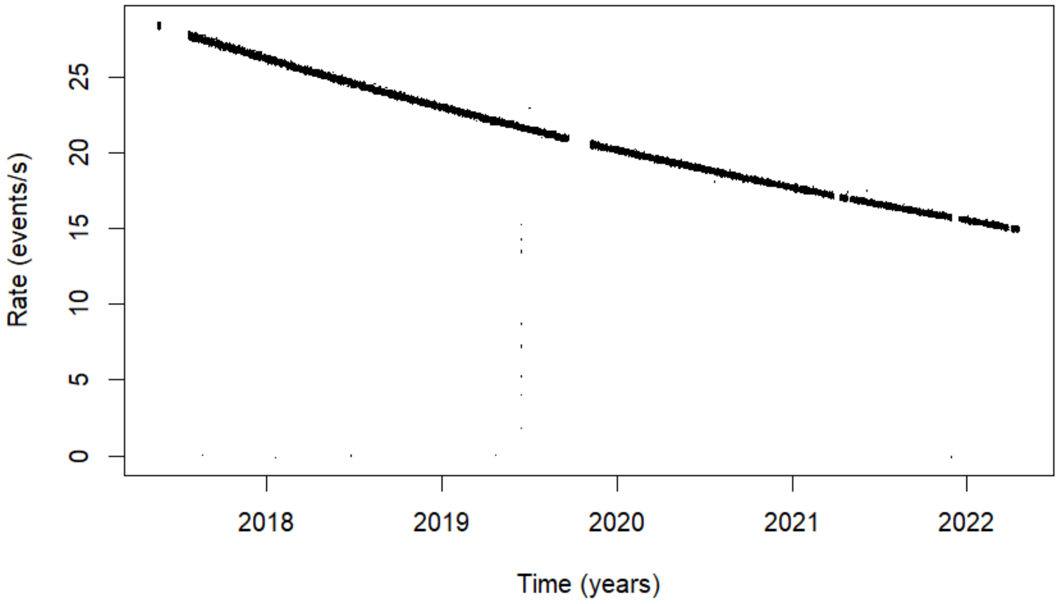

FIGURE 6: Decay rate of ^{60}Co plotted with preprocessed raw data as a function of time.

The original data as shown in Fig. 6 includes 39'444 data points. Seventeen data points with rates ≤ 14 and ≥ 30 were classified as visually implausible outliers and were manually removed. The new dataset contains 39'427 data points.

Next, an exponential function was fitted to the data. This forms the basis for calculating the residuals, which are necessary for subsequent data cleaning steps. To fit the model we use:

$$R(t) = A_0 \cdot e^{-\lambda t}, \tag{8}$$

where A_0 is the initial value or amplitude of the rate, R, at a given time, λ is the decay constant and t is the elapsed time measured from the initial point whose rate is A_0. Fig. 7 displays the manually cleaned data and the fitted exponential model with the fit parameters $\lambda = 0.131(3)$ year^{-1} and $A_0 = 28.4(2)$ events/s.

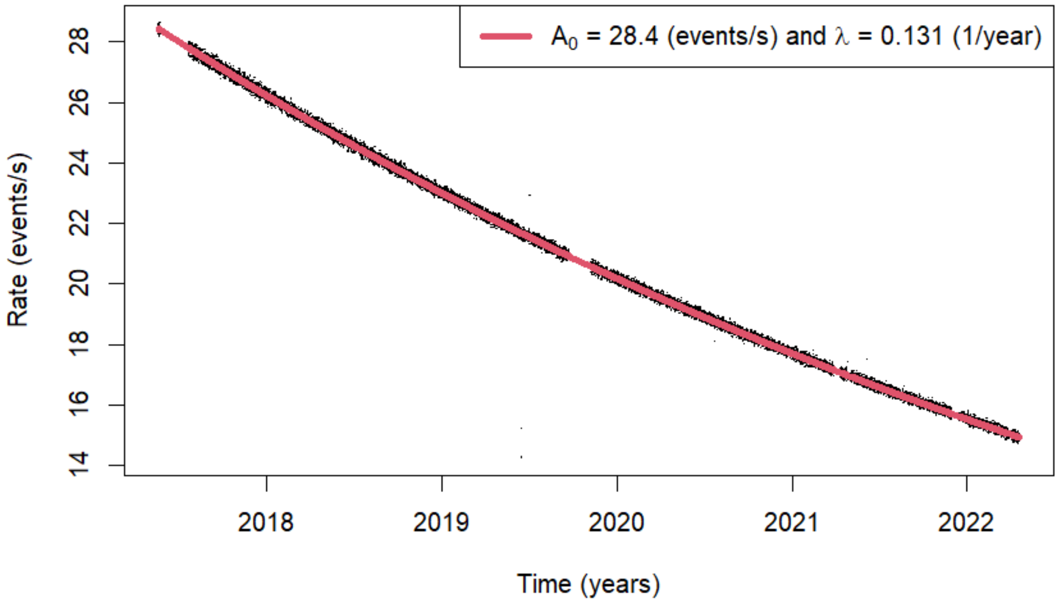

FIGURE 7: Cleaned data after the manual removal of unphysical outliers with an exponential model fitted to the data. Fit parameters $\lambda = 0.131(3)$ year^{-1} and $A_0 = 28.4(2)$ events/s.

4.1.2 Residuals and uncertainties in the rate

Based on the parameters of the exponential fit (Fig. 7), a data point was generated for each time stamp in order to compute the residuals, r_i, between the fit and the actual data, which is calculated as

$$r_i = R_i - f_i \quad \text{for } i = 1, 2, \ldots, n, \tag{9}$$

where R_i are the actual measured data points and f_i are the rates at individual time stamps obtained from the exponential fit. The individual time stamps t_i were already provided by the preprocessed raw data. To calculate f_i, the following function with the parameters A_0 and λ from the exponential fit was used:

$$f_i = A_0 \cdot e^{-\lambda t_i}. \tag{10}$$

The range of the residuals extends from -7.42 to 1.40 counts/s. The residuals are normally distributed with a mean value of $\mu = 0.003$ counts/s and a standard deviation of $\sigma = 0.107$ counts/s. Figure 8 shows the histogram of the residuals from all data points. Given that the range of the residuals is notably larger than the standard deviation from the mean, the x-axis was confined to -1 to 1 for improved visualization, using 250 bins.

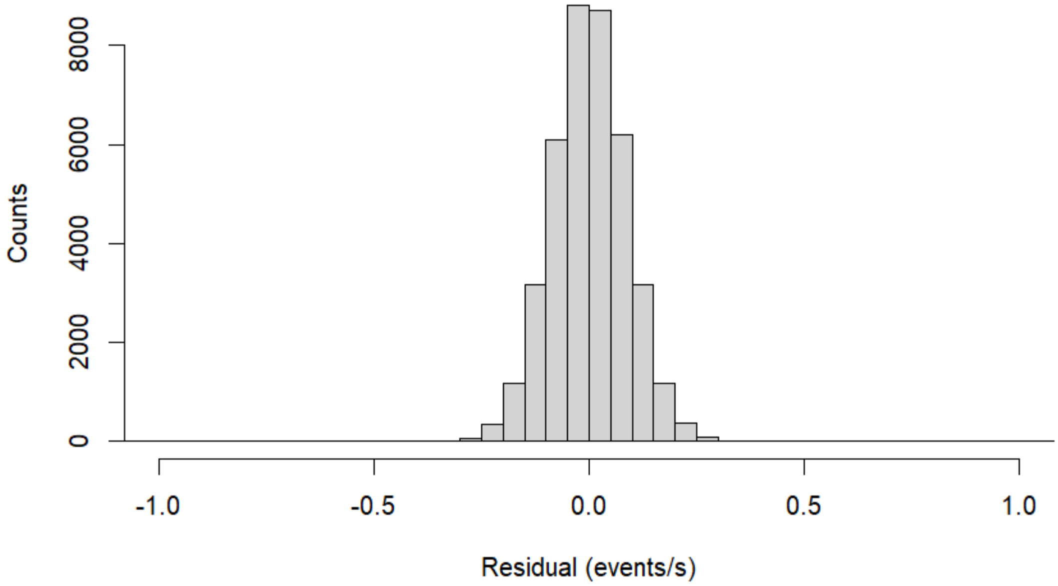

FIGURE 8: Histogram of the distribution of the residuals.

Based on the computed residuals, a threshold of four standard deviations ($4\sigma = 4\times0.107 = 0.428$ counts/s) was defined, and data points whose residuals exceed this threshold were removed. This large threshold ensures that only data points with significant statistical fluctuation were removed, and no information regarding potential modulations and signals was lost. In total, six data points were additionally removed.

During the processing of the raw data, an uncertainty, σ_R, of the rate was computed for each data point. The uncertainty was computed using error propagation including the influences of background radiation [12]. Similar to the rate, the rate uncertainty also decreases exponentially.
To better understand the behavior of σ_R, a new coefficient, Q_{σ_R}, is introduced. Each σ_{R_i} is divided by the corresponding rate R_i:

$$Q_{\sigma_{R_i}} = \frac{\sigma_{R_i}}{R_i}. \tag{11}$$

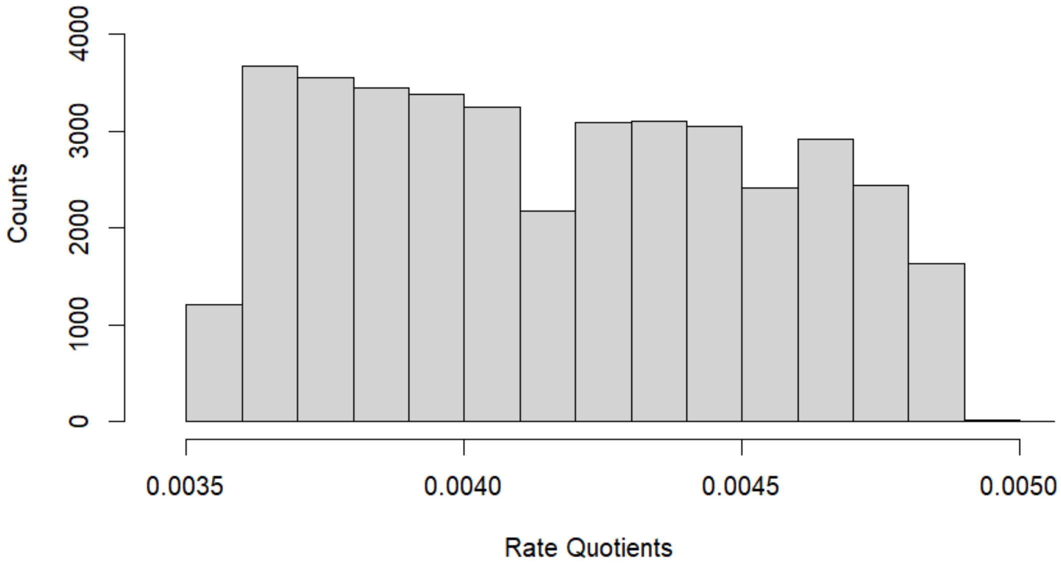

FIGURE 9: Histogram of the ratio, Q_{σ_R}, between the rate and the rate uncertainty for every data point (Eq. 11).

Figure9 shows the histogram of Q_{σ_R}. Q_{σ_R} is approximately uniformly distributed and ranges from 0.0035 to 0.005. The uniform distribution arises because Q_{σ_R} slightly increases over time. Since the basis of the data cleaning is formed by the residuals, r_i, it must be verified that the residuals follow the same behavior as the uncertainties on the rate and no data points are mistakenly classified as outliers. Therefore a quotient for the residuals Q_{r_R} was computed as well, using

$$Q_{r_{Ri}} = \frac{r_i}{R_i}. \tag{12}$$

The mean value μ and the standard deviation σ of the two quotients are shown in Tab. 5. The mean value and the standard deviation for Q_{σ_R} and Q_{r_R} are of the same order of magnitude. Since the data cleaning was conducted with a four-σ threshold of the residuals, which corresponds to a value of 0.428 counts/second, and the rate errors are in a range of approximately 0.07 to 0.12 counts/s, no data point that was previously removed has an uncertainty that lies outside the four-σ threshold.

	μ	σ
Q_{r_R}	0.0028	0.0005
Q_{σ_R}	0.0042	0.0005

TABLE 5: Mean value and standard deviation of the quotients of the rate uncertainties σ_R and residuals r_R divided by the rate R.

4.1.3 Coverage and data quality

After the data cleaning stage, where 17 data points were removed as visual outliers, and statistically informed treatment eliminated additional six data points, the final dataset is shown in Fig. 10. The distinctions in the plot are as follows:

- Total measurement period (between the black solid and the black-green dashed lines);
- Total measurement period excluding the first gap (between the green solid and the black-green dashed lines);
- First period (blue data points);
- Second period (red data points).

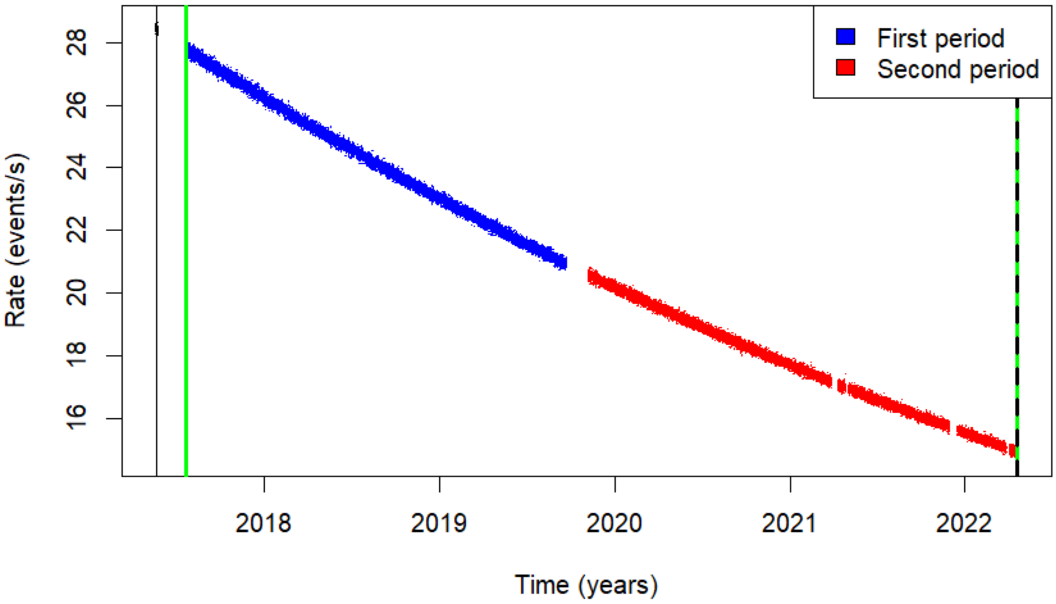

FIGURE 10: Overview of the observation periods.

The vast majority of the processed raw data is binned in 60-minute intervals. In fact, more than 99% of the time gaps between two consecutive data points are between 60.00000 and 60.00003 minutes. However, Fig. 10 includes some evident and large gaps, which resulted from technical issues interrupting the data-taking for several days. To investigate the data quality, and for further studies in the frequency domain, we defined T_{tot} as the total number of days for each period, G_{tot} as the sum of all gaps larger than 24 hours, and S_{r} as the sampling rate in hours. The coverage C in percentage is computed by

$$C = \left(1 - \frac{G_{\text{tot}}}{T_{\text{tot}}}\right) \cdot 100\%. \tag{13}$$

Table 6 shows the values of the defined variables for the different periods in Fig. 10. As expected, the coverage for the first period (blue) is the highest, and the sampling rate coincides best with the 60-minute bins from the data processing. On the other hand, the total period including the first gap has the worst coverage and deviates the most from the sampling rate of one hour.

	T_{tot} (days)	G_{tot} (days)	C(%)	S_{r} (hours^{-1})
Total period including first gap	1796.93	151.46	91.571	0.914
Total period excluding first gap	1734.25	92.41	94.672	0.945
First period	794.05	4.15	99.477	0.991
Second period	893.98	42.03	95.298	0.953

TABLE 6: Summary of values for T_{tot}, G_{tot}, C, and S_{r} for different observation periods.

The number of additional data points for including versus excluding the first gap is 88, which corresponds to approximately ∼0.2% of the total data points, whereas the difference in the coverage corresponds to ∼3.1%. Therefore, further analysis will be conducted without the first 88 data points before the large gap in 2018 (see gap Fig. 10 between the first black and first green vertical line).

4.1.4 Adjusted rate

By introducing an adjusted rate, R_{adj}, the effects of the exponential decay are neutralised. This allows for the investigation of potential seasonal fluctuations in the amplitude decoupled from the exponential component. The rate at each data point is multiplied by the corresponding positive exponent using

$$R_{adj_i} = r_i \cdot \exp(\lambda \cdot t_i), \tag{14}$$

where r_i is the rate at time i, and λ corresponds to the previously calculated decay constant obtained from the exponential fit by using Eq. 8. Fig. 11 shows the rate after the adjustment. Most of the data points fall within the range of 27.6 to 28.2 (events/s). The width of this band is attributed to statistical uncertainty.

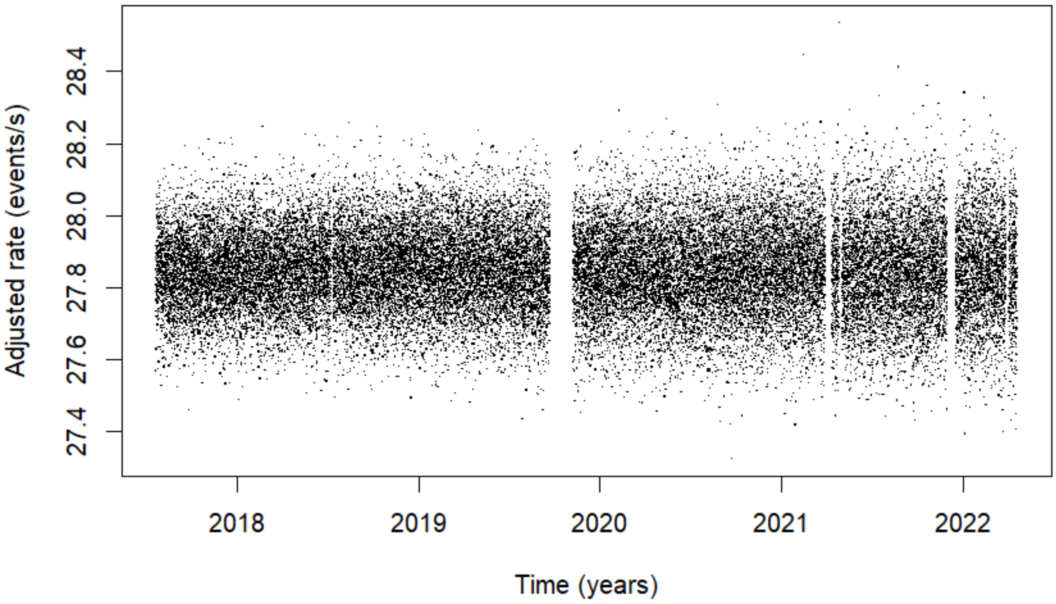

FIGURE 11: Adjusted rate after multiplying each data point by the corresponding positive component using the results obtained from the exponential fit. See text for details.

4.2 Environmental parameters

The measurement of environmental variables is an essential component of the experimental setup. Systematic errors or measurement inaccuracies may occur when environmental parameters change. If modulations in decay rates are detected, they may be attributed to modulation or seasonal effects in the measurement conditions. Table 7 provides an overview of the mean value, median, standard deviation, skewness, and kurtosis of the environmental parameters, whereas histograms and their temporal distributions are shown in Figs. 12 and 13. The measurements of the environmental parameters were taken in the inner box as discussed in chapter 3.3. The pressure (Fig. 12b) is normally distributed with a small standard deviation of approximately 0.8%. The humidity (Fig. 12c) exhibits clear seasonal fluctuations, which are most likely caused by the heating system in the laboratory, but the average humidity remained stable. There is a visible decrease of the temperature (Fig. 12e) over the course of the five-year measurement. In summer 2018, a new heating system was installed in the room. This may have led to the drastic drop in the temperature during that period. B_x, B_y, and B_z are the components of the magnetic field in the three directions of the Cartesian coordinate system. Since B_y (Fig. 13c) is constantly decreasing, while B_x and B_z remain on average constant, the overall magnetic field (Fig. 13g) shows a slight increase over the period of five years.

	Mean	Median	Sigma	Skewness	Kurtosis
Pressure (Pa)	95624.793	95676.355	773.717	-0.573	1.128
Humidity (%)	21.405	19.590	12.875	0.245	-1.079
Temperature (°C)	28.023	27.900	0.960	-0.419	2.667
B_x (mGs)	-267.969	-266.208	6.418	-1.884	7.209
B_y (mGs)	-776.609	-777.597	8.550	0.419	1.295
B_z (mGs)	-128.129	-128.033	5.093	0.842	1.597
B_{tot} (mGs)	831.527	832.324	7.639	-0.245	5.084

TABLE 7: Statistical moments of the environemtal parameters.

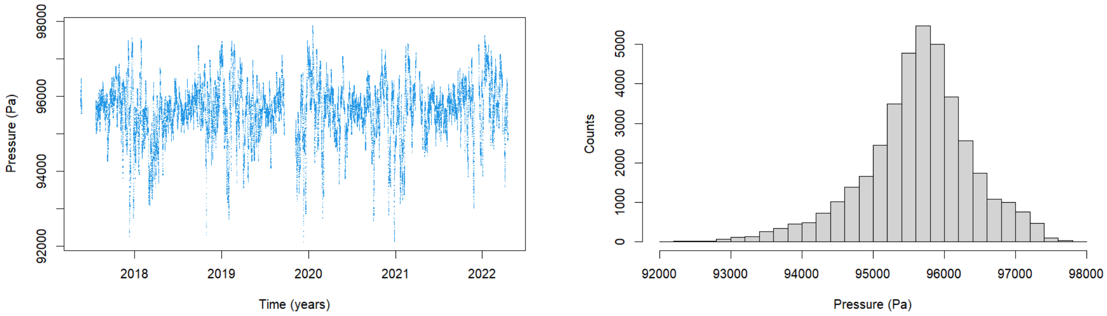

(A) Time evolution of the pressure.

(B) Histogram of the pressure.

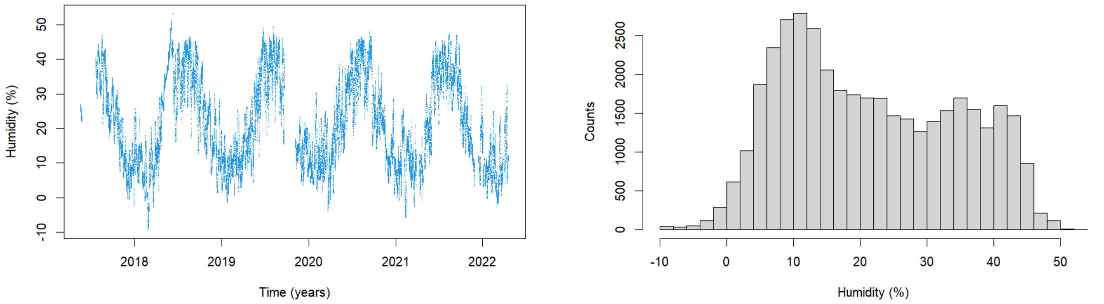

(C) Time evolution of the humidity.

(D) Histogram of the humidity.

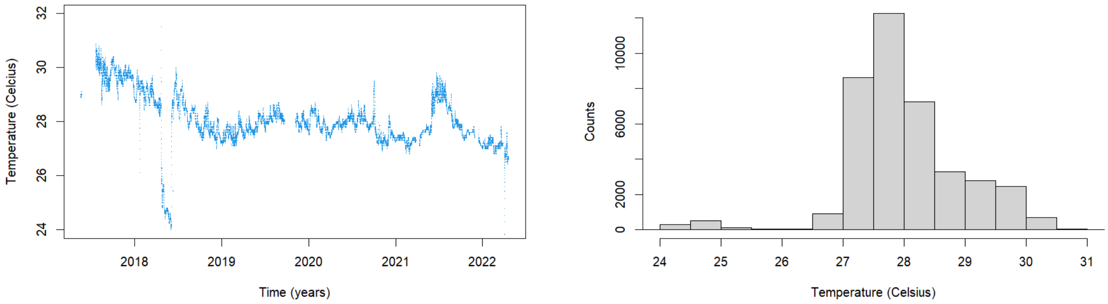

(E) Time evolution of the temperature.

(F) Histogram of the temperature.

FIGURE 12: Time evolutions and histograms of the pressure, the humidity and the temperature.

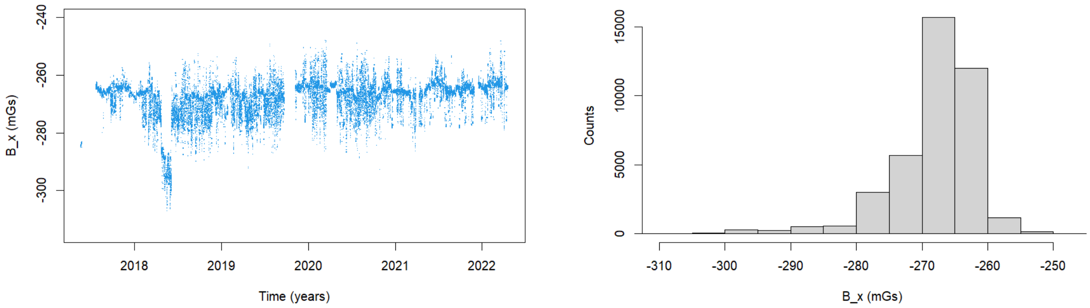

(A) Time evolution of B_x.

(B) Histogram of B_x.

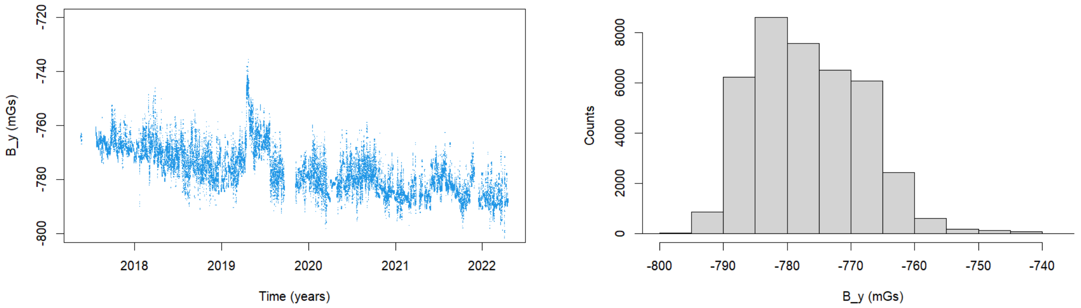

(C) Time evolution of B_y.

(D) Histogram of B_y.

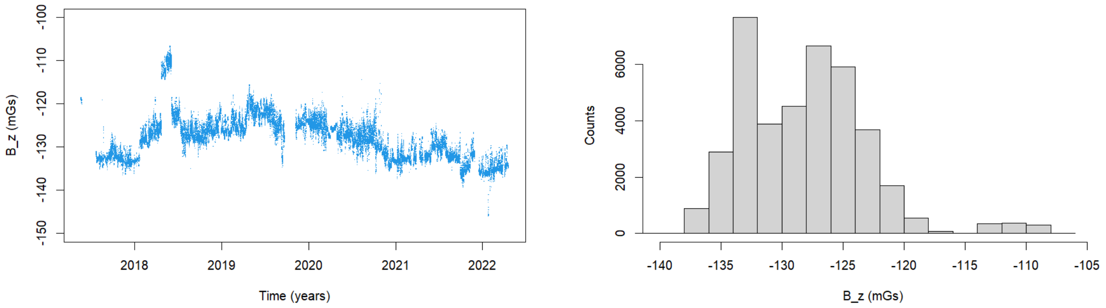

(E) Time evolution of B_z.

(F) Histogram of B_z.

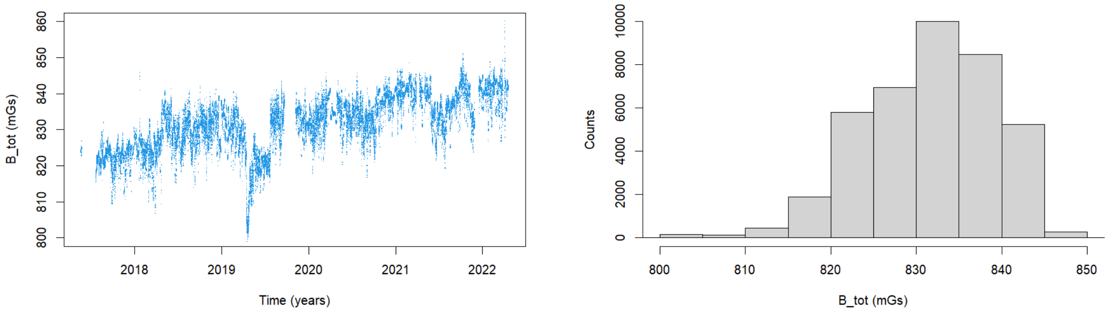

(G) Time evolution of B_{tot}.

(H) Histogram of B_{tot}.

FIGURE 13: Time evolutions and histograms of the magnetic fields.

4.3 Correlations

Changes in environmental parameters may potentially influence the accuracy of radioactive decay rate measurements. To explore this hypothesis, correlations between the adjusted rate and the environmental parameters were analyzed using the Spearman and Pearson correlation.

4.3.1 Pearson correlation

The Pearson correlation coefficient, r_p, is calculated as the covariance of the two variables divided by the product of their standard deviations

$$r_\mathrm{p} = \frac{\sum_{i=1}^{n}(x_i - \bar{x})(y_i - \bar{y})}{\sqrt{\sum_{i=1}^{n}(x_i - \bar{x})^2 \sum_{i=1}^{n}(y_i - \bar{y})^2}}, \tag{15}$$

where x_i and y_i are the individual data points, and $\bar{x}$ and $\bar{y}$ are the mean values of the investigated variables x and y, respectively [19]. The coefficient r_p represents the strength and direction of the linear relationship between two variables and ranges from -1 to 1. Positive values of r_p indicate a positive correlation, implying that an increase in one variable leads to an increase in the other. Conversely, negative values indicate a negative correlation, implying that an increase in one variable implies a decrease in the other one. Values of r_p close to 1 (and -1) indicate a strong linear positive (negative) relationship. It's important to consider the limitations and assumptions when interpreting r_p. Pearson correlation assumes a linear relationship between the variables as well as that the variables are normally distributed. Outliers can strongly influence r_p.

4.3.2 Spearman correlation

Given the relatively strict assumptions and limitations required for the use of the Pearson correlation, Spearman correlation method was used in our analysis as well. Compared to Pearson correlation, Spearman correlation is a more robust method to measure correlations between datasets. The main differences between Spearman and Pearson correlations are:

- **Linearity:** The Pearson correlation assumes linearity, while the Spearman correlation does not, making the Spearman correlation more flexible in capturing various types of relevances.
- **Sensitivity to outliers:** Pearson correlation is sensitive to outliers, while Spearman correlation is less influenced by extreme values.
- **Data types:** The requirements for the data type are higher for Pearson correlation. Pearson correlation assumes a normal distribution of the variables, while Spearman correlation does not.
- **Calculation method:** Pearson correlation operates on actual values, while Spearman correlation works with ranks. The rank refers to the position of each observation when the data is sorted in ascending order. Each observation is assigned a rank based on its position in the sorted data. Hence, the precise value is less important than the relative order between the data points.

The Spearman correlation is computed with

$$r_\mathrm{s} = 1 - \frac{6\sum d_i^2}{n(n^2-1)}, \tag{16}$$

where d_i is the difference between the ranks of corresponding pairs of variables and n (=39'421 data points) is the number of observations [19].

4.3.3 Correlation matrices

The results of the computation of the Pearson and the Spearman correlation models for the "total period excluding first gap" (see Fig. 10) are shown in Fig. 14. Neither of the two models shows any correlations between the adjusted rate and any of the environmental parameters. For the other examined periods, nearly identical results are obtained.

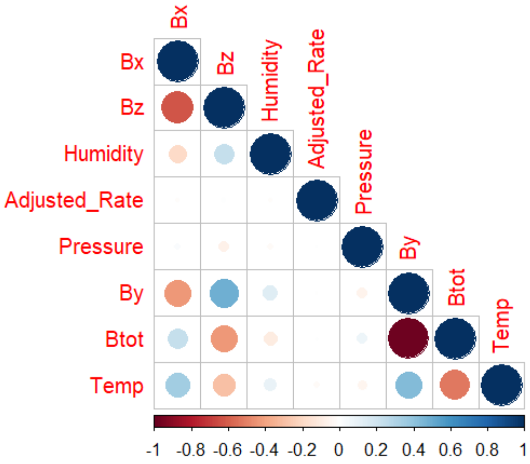

(A) Pearson correlation matrix

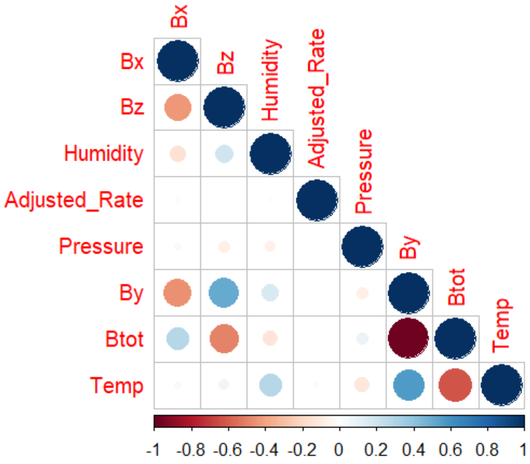

(B) Spearman correlation matrix

FIGURE 14: Pearson and Spearman correlation matrices with data from "total period excluding first gap" (see Fig. 10). No correlation between the adjusted rate and any of the environmental parameters is observed.

4.4 Fourier analysis of the adjusted rate

4.4.1 Adjustment of sampling rate

As shown in Tab. 6, the three periods under investigation exhibit different coverages and sampling rates. This leads to shifts in the frequency spectrum when applying a Fourier transformation (FFT). To correct for this effect, the sampling rates S_r are divided by their respective coverages C

$$S_{r_{\text{new}}} = \frac{S_r}{C}. \tag{17}$$

The resulting effect is illustrated using the example of the frequency spectrum of the pressure data as shown in Fig. 15. Before the correction, the peaks are clearly distinguishable from one another. The correction results in an alignment. The first period (blue) is the one with the highest accuracy with respect to an hourly sampling rate. Hence, the correction for the blue one is the smallest.

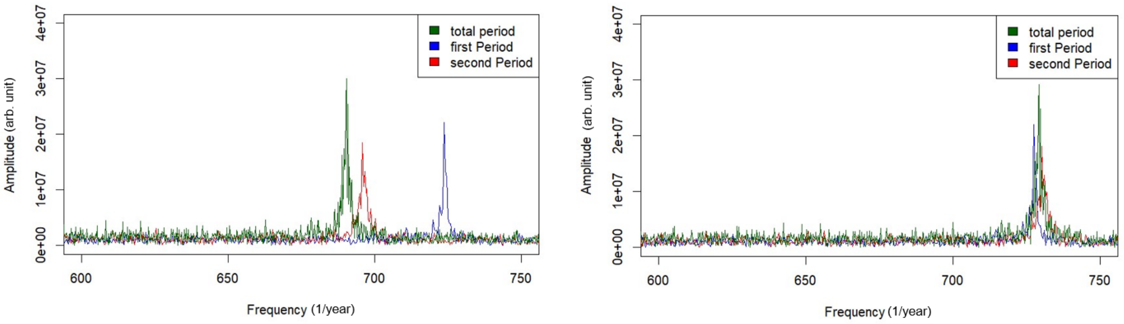

(A) Before correction.

(B) After correction.

FIGURE 15: Frequency spectrum of pressure. The left side displays the peaks before the correction. The right side shows the aligned peaks after the correction.

4.4.2 Frequency spectra and peaks

The focus of the frequency spectrum analysis is primarily on annual modulation. Figure 16 depicts the frequency spectrum of the adjusted rate. The x-axis represents the number of events per year for the three periods under investigation. No specific peaks can be identified. In comparison, the frequency spectrum of humidity as displayed in Fig. 17 shows a clear peak at approximately one event per year for all periods alike. These peaks coincide with the sinusoidal-like profile shown in Fig. 12c. The peak at 0 can be disregarded as it merely indicates that a multitude of data points are assigned to a frequency of "0 events per year".

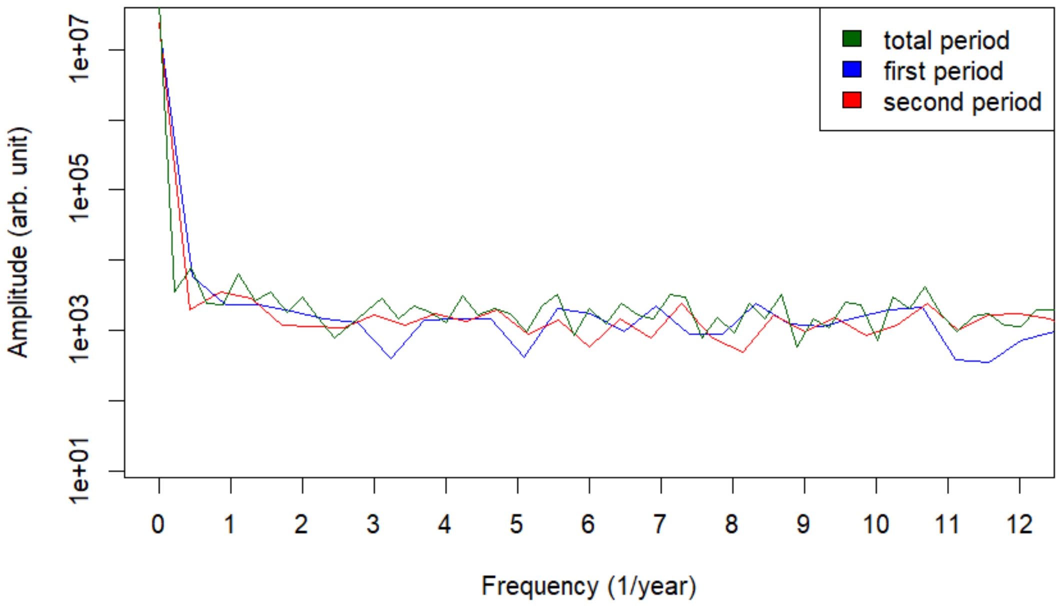

FIGURE 16: Frequency spectrum of the adjusted rate.

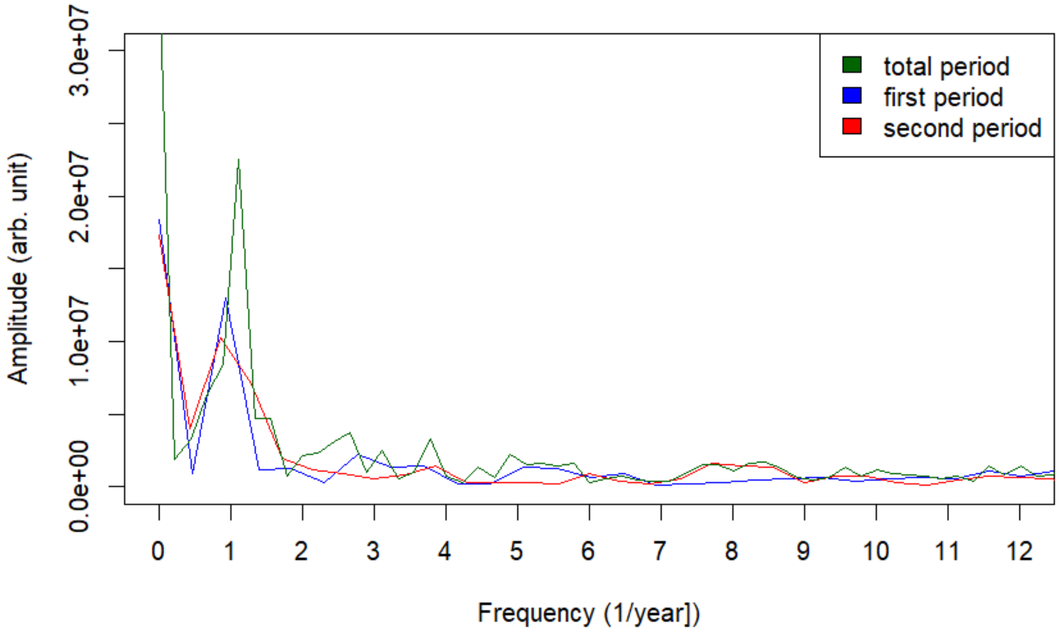

FIGURE 17: Frequency spectrum of the humidity.

In order to facilitate quantitative comparisons alongside visual observations, the amplitudes in the frequency domain are sorted by magnitude. Table 8 provides an overview of the amplitudes and the localization (events per year) of the adjusted rate for the three examined periods. Table 9 displays the analogous values for humidity.

Total period		First period		Second period	
Frequency (1/year)	Amplitude (arb. unit)	Frequency (1/year)	Amplitude (arb. unit)	Frequency (1/year)	Amplitude (arb. unit)
0.00	47476247	0.00	22814307	0.00	24661896
0.40	7958	0.50	5898	3131.70	4902
1715.00	7186	2908.00	3880	2887.30	4754
1.10	6460	903.10	3784	1718.70	4614
3041.50	6138	4362.30	3749	1587.50	4429
3735.40	6060	3432.90	3627	1801.40	4384
3262.60	5994	3136.00	3583	1530.00	4329
1232.00	5865	1926.80	3537	4126.30	4324
1551.00	5795	2589.00	3532	3484.90	4323
3606.60	5772	600.20	3491	452.70	4251
1542.10	5723	2597.80	3426	3728.90	4248
151.10	5691	3235.90	3414	2457.30	4245
2922.70	5652	299.20	3393	4278.90	4157
2608.20	5600	3736.20	3344	156.90	4115
3559.00	5579	2824.80	3335	3093.50	4087
4269.50	5573	377.80	3314	3743.40	4080
2920.70	5559	1393.70	3308	3172.80	4077
707.90	5521	52.30	3298	3867.30	4044
3143.40	5485	1351.10	3295	42.90	4029
3549.80	5460	1840.80	3276	716.80	3991

TABLE 8: Adjusted rate - FFT peaks and corresponding frequencies.

Total period		First period		Second period	
Frequency (1/year)	Amplitude (arb. unit)	Frequency (1/year)	Amplitude (arb. unit)	Frequency (1/year)	Amplitude (arb. unit)
0.00	35743655	0.00	18399089	0.00	17346236
1.11	22519273	0.92	13043657	0.86	10250097
0.89	8389856	2.77	2230580	1.29	7090438
0.67	6335475	3.70	1467287	0.43	4041014
1.56	4724161	5.09	1376826	1.71	1978338
1.33	4693018	3.24	1343818	7.72	1643199
2.67	3728025	1.85	1293825	8.15	1463023
3.78	3324141	5.55	1260673	3.86	1444320
0.44	3306071	1.39	1184191	15.00	1440923
2.45	3122896	14.33	1121441	8.57	1329511
3.11	2523092	12.48	1111575	2.14	1150561
2.22	2307924	11.56	1069633	45.01	996781
4.89	2243886	18.03	1028890	6.00	949372
2.00	2173832	15.26	995341	2.57	942174
0.22	1933398	6.47	925788	23.58	923617
8.45	1762348	0.46	923035	15.86	891485
18.02	1734058	18.96	851800	48.44	869660
15.13	1664068	26.36	841021	21.44	865670
5.78	1611061	45.32	840366	16.72	855182
16.02	1609983	40.69	830917	18.86	837440

TABLE 9: Humidity - FFT peaks and corresponding frequencies. The amplitude of the annual modulation of humidity is 20.27%, where "%" refers to the relative humidity.

Considering Tab. 9 for the "First period" and disregarding the amplitude at frequency 0, one observes that the magnitude at a frequency of 0.92 is approximately 6 times larger than the second largest value at a frequency of 2.77 (events per year). This value at a frequency of 0.92 is defined as the "first order peak". The next 11 amplitudes are all on the same order of magnitude and are defined as "second order peaks". All remaining amplitudes are classified as "lower order peaks". For the adjusted rate (Tab. 8), we categorized >5'000 peaks as "first order peaks", which are on the same order of magnitude, indicating that there is no dominant frequency in comparison with the humidity. Table 10 summarizes the number of first, second, and lower order peaks for humidity and adjusted rate for the "First period" shown in blue in Fig. 10.

Variable	**First order peaks**	**Second order peaks**	**Lower order peaks**
Adjusted rate	>5’000	>4’000	100
Humidity	1	11	>9’000

TABLE 10: Number of first, second and lower order peaks for "first period".

4.5 Half-life

To determine the half-life $t_{1/2}$ of ^{60}Co, the decay constant $\lambda = 0.131(3)$ year^{-1} obtained from the fit in Fig. 7 is utilized. The half-life is then computed using

$$t_{1/2} = \frac{\ln(2)}{\lambda}. \tag{18}$$

The uncertainty, $\delta t_{1/2}$, of $t_{1/2}$ is computed using

$$\delta t_{\frac{1}{2}} = \left| \frac{dt_{\frac{1}{2}}}{d\lambda} \right| \cdot \delta\lambda, \tag{19}$$

where $\delta\lambda$ corresponds tho the uncertainty of the decay constant. As displayed in Tab. 11 the calculated value for $t_{1/2}$, along with its uncertainty, falls within the range of the literature value.

	Computed (y)	Literature value (y) [20]
$t_{1/2}$	5.3(1)	5.2712(4)

TABLE 11: Comparison of computed half-life and literature value.

5 Conclusion

This thesis focuses on exploring correlations between environmental parameters and the decay rate of ^{60}Co. It also includes a frequency spectrum analysis to investigate potential periodicity on the decay rate of ^{60}Co. Two different methods (Pearson and Spearman correlation) were employed to investigate the relationship between the rate and the environmental parameters such as humidity, magnetic field, temperature, and pressure. Both yielded nearly identical results, indicating no correlation between the decay rate and any of the environmental parameters. The frequency analysis was performed using Fourier transformation. Neither visually nor quantitatively were significant frequencies identified that would suggest modulation or indicating any pattern in the decay rate. This especially holds for annual modulations. In conclusion, the results of this thesis suggest that there is no modulation in the decay rate of ^{60}Co and the half-life extracted from our data gives $t_{1/2} = 5.3(1)$ years, which is consistent with the literature value of 5.2712(4) years.

6 Outlook

There are several avenues for further investigation. Datasets from other channels and energy peaks, as well as the data from the other three universities, should be examined. This will not only enhance the scope of analysis but also facilitate cross-validation of findings. Furthermore, a statistical limit on the modulation amplitude can be determined using the existing data. Additional statistical methods such as moving average and other models to fit the data can be applied to improve the statistical uncertainty of the analysis. Furthermore, studies on systematic uncertainties should be considered to decompose the uncertainty of the fit result of the extracted half-life of ^{60}Co.

7 Declaration

I hereby confirm that I have written this thesis independently. All sources and third-party intellectual property have been marked as such. Online translation- and correction-tools were used for the translation from German to English and the grammatical correction.

8 Acknowledgements

I dedicate this thesis to my parents - especially my mother for her years of unwavering support. I would like to thank Professor Laura Baudis for giving me the opportunity to write this thesis in her research group. Additionally, a big thank you goes to Dr. Pin-Jung Chiu and Dr. Yannick Müller. Both have accompanied me from the beginning and have always patiently and helpfully supported me. I also want to thank the entire research group of Prof. Baudis for their inputs and support.

References

[1] D. Jenkins, *Radiation Detection for Nuclear Physics* (IOP Publishing Ltd, ISBN 978-0-7503-1429-9, 2020).

[2] D. Alburger, G. Harbottle and E. Norton, “Half-life of ^{32}Si”, Earth and Planetary Science Letters **78**, 168–176 (1986).

[3] J. H. Jenkins et al., “Evidence of correlations between nuclear decay rates and Earth–Sun distance”, Astroparticle Physics **32**, 42–46 (2009).

[4] E. N. Alexeyev et al., “Results of a search for daily and annual variations of the ^{214}Po half-life at the two year observation period”, Physics of Particles and Nuclei **47**, 986–994 (2016).

[5] E. B. Norman, E. Browne, H. A. Shugart, T. H. Joshi and R. B. Firestone, “Evidence against correlations between nuclear decay rates and Earth–Sun distance”, Astroparticle Physics **31**, 135–137 (2009).

[6] E. Bellotti, C. Broggini, G. Di Carlo, M. Laubenstein and R. Menegazzo, “Search for time dependence of the ^{137}Cs decay constant”, Physics Letters B **710**, 114–117 (2012).

[7] J. Angevaare et al., “A precision experiment to investigate long-lived radioactive decays”, Journal of Instrumentation **13**, P07011–P07011 (2018).

[8] W. Demtröder, *Experimentalphysik 4* (Springer Berlin Heidelberg, ISBN 978-3-662-52883-9, 2017).

[9] The Nobel Prize in Physics 1903, *NobelPrize.org. Nobel Prize Outreach AB 2023. Thu. 28 Sep 2023. https://www.nobelprize.org/prizes/physics/1903/summary/.*

[10] B. Povh, K. Rith, C. Scholz, F. Zetsche and W. Rodejohann, *Particles and Nuclei* (Springer Berlin Heidelberg, ISBN 978-3-662-46320-8, 2015).

[11] H. Siegert, H. Schrader and U. Schötzig, “Appl. Radiat. Isot. 49 1397.”, (1998).

[12] Stefanie Javet, *Data processing and analysis of the modulation experiment, Bachelor thesis, University of Zurich*, 2019, https://www.physik.uzh.ch/en/groups/baudis/Publications/Theses.

[13] C. Grupen and B. Shwartz, *Particle Detectors* (Cambridge University Press, ISBN 978-1-009-40153-1, Mar. 2008).

[14] W. Demtröder, *Experimentalphysik 3* (Springer Berlin Heidelberg, ISBN 978-3-662-49093-8, 2016).

[15] M. Gienal, *Characterization of NaI(Tl) detectors for a radioactive decay rate modulation search experiment, Bachelor thesis, University of Zurich*, Zurich, 2017, https://www.physik.uzh.ch/en/groups/baudis/Publications/Theses.

[16] Peter R. Barrow, “Searching for Dark Matter with XENON100, Research and Development for XENON1T, and Modulating Radioactive Decay Rates”, PhD thesis (University of Zurich, Zurich, 2016, https://www.physik.uzh.ch/en/groups/baudis/Publications/Theses).

[17] CAEN DT5533P Manual, *https://www.caen.it/products/dt5533e/.*

[18] J. Angevaare et al., “No correlation between Solar flares and the decay rate of several β-decaying isotopes”, Astroparticle Physics **103**, 62–66 (2018).

[19] A. Handl and T. Kuhlenkasper, *Einführung in die Statistik* (Springer Berlin Heidelberg, ISBN 978-3-662-56439-4, 2018).

[20] E. Browne and J. Tuli, “Nuclear Data Sheets for A = 60”, Nuclear Data Sheets **114**, 1849–2022 (2013).